

Internal wave and turbulence observations with very-high resolution temperature sensors along the Cabauw tower

by

Hans van Haren^a, Fred. C. Bosveld^b

^aRoyal Netherlands Institute for Sea Research (NIOZ), P.O. Box 59, 1790 AB Den Burg, the Netherlands.

^bRoyal Netherlands Meteorological Institute (KNMI), P.O. Box 201, 3730 AE De Bilt, the Netherlands.

Corresponding author: Hans van Haren, hans.van.haren@nioz.nl

ABSTRACT

Knowledge about the characteristics of the atmospheric boundary layer are vital for the redistribution of air and suspended contents that are particularly driven by turbulent motions. Despite many modelling studies, detailed observations are still demanded of the development of turbulent exchange under stable and unstable conditions. In this paper we present an attempt to observationally detail atmospheric internal waves, under stable conditions, and associated turbulent overturning, under quasi-stable and unstable conditions. Therefore, we mounted 198 high-resolution temperature ‘T’-sensors on a cable. The instrumented cable was attached along the 213 m tall mast of Cabauw, the Netherlands, during late-summer 2017. The mast has standard and special meteorological equipment at extendable booms every 20 m in height. A sonic turbulence anemometer is at 60 m above ground. The extra, originally underwater-, T-sensor cable was suspended down from the 206-m level, temporarily for about 3 months. While in water the sensors have a response time of $\tau_w \approx 0.4$ s and drift of $0.001^\circ\text{C}/\text{mo}$, in air the response time $\tau_a \approx 3$ s is relatively slow and the apparent drift of about $0.1^\circ\text{C}/\text{mo}$ relatively large. Least performance is during daytime. These T-sensor characteristics hamper quantitative atmospheric turbulence research, as it results in a relatively narrow inertial subrange of only one order of magnitude. Nevertheless, height-time images from two contrasting days show common nocturnal marginally stable density stratification supporting internal waves up to the buoyancy period of about 300 s, shear and convective deformation of the stratification over the entire 197 m range of observations.

KEYWORDS: Boundary-layer meteorology; High-resolution temperature sensors; Internal waves; Mast observations; Stratified turbulence

1. Introduction

The dynamics of atmosphere and ocean are quite alike, with convective turbulent overturning and internal waves supported by stable vertical density stratification on the small scales, cyclones and eddies on the mesoscales and global circulation on the large scales. There is one crucial difference between their dynamics in that the ocean is mainly heated by daytime solar insolation from above, while the lower atmosphere from below. The former results in a stable vertical density stratification, while the latter leads to unstable conditions as warm air/water is less dense than cold air/water. Under stable conditions, turbulent exchange is hampered in the vertical, with the more dominant process of diapycnal turbulent mixing being wind/current shear driven. Under unstable conditions, the dominant vertical turbulent exchange is via convection. As a result, ocean dynamics are more akin to an environment with a poor heat engine while the atmosphere is a more effective heat engine (Peixoto and Oort 1992; Munk and Wunsch 1998).

As the ocean is mainly stably stratified in density, internal gravity waves dominate the kinetic energy and are thus, paradoxically, crucial for generating turbulent overturning and vertical diapycnal mixing. A prominent source of such turbulent overturning is via internal wave breaking above sloping topography (Eriksen 1982; Thorpe 1987). Because of their dominance, internal waves are well studied in the ocean.

In the atmosphere, internal gravity waves, sometimes shortened to ‘gravity waves’ or ‘internal waves’, are abundant in the upper layers above the mesopause at about 90 km above ground where temperature is increasing with height (Xu et al. 2007; Nappo 2012). Below the mesopause they are found in diverse layers like in the stratosphere. In the lower atmosphere of the planetary boundary layer, breaking internal waves are

expected to be less important for turbulent exchange as daytime convection is a more dominant source of turbulence that can extend up to the tropopause at about 12 km above ground (e.g., Schenk 1974; Gettelman et al. 2002). Nevertheless, tropospheric internal waves are known to exist, as the troposphere is often stably stratified due to the action of radiation divergence. More specifically, internal waves occur during nocturnal periods in its lowest few 100 meters when radiative surface cooling stabilizes the atmosphere. Internal waves are for instance excited over mountains (Alexander et al. 2007; Akylas 2010; Conrick et al. 2018; La et al. 2020). Several qualitative studies using acoustic and lidar imaging have demonstrated such internal waves (e.g., Fritts and Anderson 2003; Nappo 2012).

In this paper, we present an observational study on the behavior of internal waves in the stable atmospheric planetary boundary layer. The instrumentation used here has been developed for measuring internal wave-induced turbulence in the ocean, and we want to address its usefulness for measuring in the atmosphere. For this purpose, a 213 m tall meteorological mast was equipped with 198 temperature sensors sampling at a rate of 1 Hz in late summer. We also seek to compare ocean internal wave - turbulence structures with those in the lower atmospheric boundary layer.

2. Linear and nonlinear internal waves and stratified turbulence

As in weakly stable surface layers transport is dominated by turbulence, Monin-Obukhov scaling works well to describe vertical transport as a function of the atmospheric state variables. However for very stable cases this formalism appears to break down (Holtslag et al. 2013). In the review paper by Sun et al. (2015) it is noted that under such conditions shear generation of turbulence is significantly suppressed. Thus, the interaction between internal gravity waves and turbulence may become

important. Internal gravity waves are known to be excited by topography (e.g., Steeneveld et al. 2009). But even under relatively flat conditions these waves may emerge from smaller scale surface obstacles. For example, they may result from the action of low-level jets at the top of the stable atmospheric boundary layer, or from the action of density currents related to processes higher up in the atmosphere or from distant topography. Sun et al. (2015) use the term “dirty waves” to indicate that in reality waves often have characteristics which are far off from the ideal waves, in terms of length and constant amplitudes on which our theories are based. They also note that observations that shed light on the interaction between internal gravity waves and turbulence are scarce.

Internal waves are supported by the density stratification up to the buoyancy, aka Brunt-Väisälä, frequency, the natural frequency of oscillation in a stratified fluid (Groen 1948), for the atmosphere defined by (e.g., Tsuda et al. 1991),

$$N = (g/\theta \cdot d\theta/dz)^{1/2}, \quad (1)$$

where g denotes the acceleration of gravity, $\theta = T \cdot (p_0/p)^\kappa$ the potential temperature in K, T the measured absolute temperature, p the pressure and $p_0 = 10^5 \text{ N m}^{-2}$ a reference pressure. The Poisson constant reads $\kappa = (R/c_p) \cdot (1 - 0.24r_v)$, for gas constant R , specific heat at constant pressure c_p and water vapor mixing ratio $r_v = Q/(1-Q)$ for specific humidity Q (in kg kg^{-1}). In dry air, $r_v = 0$ and $\kappa = 0.2854$. The measurement of the buoyancy frequency via vertically detailed temperature observations supported by general atmospheric observations may thus indicate the possible existence of internal waves, at frequencies $\sigma < N$, and/or turbulence induced by wave breaking, at $\sigma > N$. This separation can be understood as turbulence scales being suppressed at time-scales $> T_N = 2\pi/N$ and internal waves not being able to propagate freely when their periods are $< T_N$.

Matters become complex in a varying environment in which N also varies in space and time. Ideally, N is determined from averaging over all turbulence spatial and temporal scales. If these scales are unknown, N may be conservatively calculated over all internal wave scales, given below. In the lower atmosphere near the planetary boundary, nocturnal quantitative temperature and other meteorological measurements have revealed internal waves (e.g., de Baas and Driedonks 1985; Finnigan 1988; Duynkerke 1991). The cited references refer to ‘Kelvin-Helmholtz (internal) wave’, which is understood as a particular nonlinear wave-type.

In contrast, following Carpenter et al. (2011), we refer to linear internal waves, as non-interacting waves that are mainly driven by buoyancy forces and that can freely propagate at frequencies in the band $f \leq \sigma \leq N$ (e.g., Groen 1948; LeBlond and Mysak 1978), where f denotes the inertial frequency, the vertical component of the local Coriolis frequency. As the ‘background stratification’ N determines the fate of the entire internal wave band, it should be calculated from averages over the inertial period of half a pendulum day in time, and over several tens of meters in the vertical for typical internal wave amplitudes in the lower atmosphere. Length scales matter, and large-scale waves may deform N via straining in locally thin strongly stratified layers separated by more homogeneous layers above and below. Such layering can be persistent in time and horizontal space to the extent that it can support small-scale, high-frequency internal waves at $N_s > N$.

Linear waves transfer momentum, but not mass or matter. In principle, one expects their spectral appearance to peak with limited bandwidth if the source has a deterministic frequency. In ocean observations, the internal wave band is spiked around tidal harmonic frequencies. However, in geophysical environments the supporting stratification varies in time and space over a broad range of scales and

causes a wide distribution of energy with frequency resulting in strong ‘intermittency’ with time for internal waves in general. Thus, under such conditions linear waves can become nonlinear waves that will deform and may break and generate turbulent overturning whereby mass and matter are transported.

When nonlinear waves are generated via interaction with wind/current by the process of shear instability they are named Kelvin-Helmholtz instability ‘KHi’, or vorticity generated waves. Other forms of nonlinear waves are, e.g., solitary waves and waves generated following Holmboe instability. The KHi are an important route for transferring energy from linear internal waves to turbulence in the ocean (e.g., Smyth and Moum 2012).

KHi generation may be computed from the one-dimensional shear flow stability analysis of Miles (1961) and Howard (1961). Depending on the viewpoint, stabilizing stratification or destabilizing shear, a criterion is defined when internal waves are supported or turbulence is generated. By indicating the ratio between the regimes of stabilizing stratification and destabilizing shear, the (bulk) gradient Richardson number is defined as,

$$Ri = N^2/S^2, \quad (2)$$

in which $S = ((\partial u/\partial z)^2 + (\partial v/\partial z)^2)^{1/2}$ denotes the vertical shear-magnitude of (wind) vector $\mathbf{W} = [u, v]$. In a one-dimensional shear flow the two regimes dominate above and below a ‘critical’ $Ri_{cr} = 0.25$, respectively. Following this stability analysis, KHi may develop for $Ri < 0.25$. In the ocean, the essentially three-dimensional background and (nonlinear) internal wave interactions yield a transitional Ri-value of 1 between stable ($Ri > 1$) and unstable ($Ri < 1$) regimes (Abarbanel et al. 1984), leaving a condition of ‘marginal stability’ for values in the range $0.25 < Ri < 1$ (van Haren et al., 1999).

Duynkerke (1991) analysed standard meteorological observations sampled at once per 10 min during a summertime shallow fog night. This sampling rate resolved ‘internal waves’ with typical periods of 40 min, which were also observed over mountainous terrain by La et al. (2018). Distinction was observed in the lower 30 m above ground where radiation fog was found, together with stronger stratification and ‘oscillatory’ motions near the buoyancy frequency that were trapped in the layer up to 60 m above ground (Duynkerke 1991).

While internal waves have been mostly revealed in the nocturnal atmospheric boundary layer, turbulence intensity was not found negligible (Nieuwstadt 1984). Although Nieuwstadt (1984) focused on planetary-surface frictionally induced turbulence, an alternative suggestion may be internal wave breaking in the stable nocturnal stratification. Frehlich et al. (2008) demonstrated ‘stably stratified turbulence’ with dissipation rates between 10^{-5} and $10^{-3} \text{ m}^2 \text{ s}^{-3}$ over 250 m of the atmospheric boundary layer using high-frequency profiling instrumentation and lidar.

Results from extensive arrays of 34 thermocouples and 6 sonic anemometers sampling at rates $O(10)$ Hz the lower 60 m of the atmospheric boundary layer have been reported by Burns and Sun (2000) and Sun et al. (2012). Their analyzed data were also (sub-)sampled at 10 min and yielded similar results as in Duynkerke (1991). For detailed quantitative studies on the transition from atmospheric internal waves to turbulence one has to sample faster for prolonged periods of time of several weeks, as has been done using instrumentation resolving the buoyancy period by a factor of 100 in the ocean (e.g., van Haren and Gostiaux 2012). This may be feasible using distributed temperature sensing ‘DTS’ from optic fibre techniques in the atmosphere, suspended from a balloon (e.g., Keller et al. 2011) or attached to a mast (Peltola et al. 2021).

3. Experimental setting and data handling

a. Mast set-up



Fig. 1. View from the north of the entire KNMI-mast in Cabauw in summer, and, in the foreground, from the south and from below in autumn-fog with lower end of temperature T-sensor cable suspended along-side (the red arrow points at a T-sensor).

For 50 years, the Royal Netherlands Meteorological Institute ‘KNMI’ operates a 213 m high guyed mast (Fig. 1) for atmospheric boundary layer research located in the flat grasslands of Cabauw, the Netherlands, at 51.971°N , 4.927°E (Bosveld et al.

2020). The mast has permanent standard and special meteorological equipment mounted at 9.4 m long extendable booms every 20 m height level. Instruments can be reached from intermediate platforms around the mast by moving the booms to their respective service level. 1 minute mean wind, temperature, and humidity observations are obtained at 2, 10, 20, 40, 80, 140, and 200 m above ground. The mast is also equipped with a Gill R3 sonic anemometer/thermometer for turbulence observations at 60 m above ground. The ‘sonic’, as it is called in short, samples at a rate of 10 Hz and has a verified time constant of <0.1 s, so that it resolves turbulence scales down to about 0.5 m. In a field 200 m north of the mast, surface energy budget observations are performed. These energy budget observations include in- and outgoing short- and long wave radiation, and the fluxes of momentum, heat, and water vapor.

For the specific study of internal wave turbulence in the atmospheric boundary layer, a Royal Netherlands Institute for Sea Research ‘NIOZ’ temperature ‘T’-sensor string was temporarily mounted on a cable and suspended from the 206 m service level to the roof of the mast’s main building. For safety and logistics reasons, the T-string cable was positioned on the south-side of the tower, fixed against the outside of intermediate platforms at a distance of 1.6 m from the 2 m diameter mast (Fig. 1). The T-string, which consisted of two sections, was led along the edge of the service and boom levels between the south guy and the south-east booms. The T-string was hoisted into the tower after lowering a pulley with hoist line from the 206 m level to the ground, pulling it up by hand and attaching the hoist line to a car. Driving the car away from the mast pulled the T-string up. One T-string-section of 99 m was placed between the 206 and 106 m service levels and another section of 100 m between the 106 m level and about 2 m above the roof of the main building. The lowest sensor was thus at $z = 7$ m, the highest at $z = 204$ m. The two sections were connected at the 106

m level. At the top of the roof, a 200 kg weight was placed and a tension band was used to secure the cable. This operation was performed on 14 August 2017 (yearday 225, using the convention that 1 January 1200 UTC = 0.5 yearday). The mounting was secured to be able to withstand a hurricane, in theory. The T-string was lowered by hand via a pulley to the ground on 29 November 2017.

b. Temperature sensors

Before mounting the cable in the tower, 198 NIOZ4 T-sensors were taped to the nylon-coated steel cable at 1 m intervals. The T-sensors sampled at a rate of 1 Hz. This sampling rate is considerably faster than the typical nocturnal buoyancy period $T_N > 100$ s, so that large-scale turbulent overturns having time-scales between 2 and 100 s are expected to be resolved, besides internal waves. The sampling was synchronized to a single standard clock inductively every 4 hours, so that an entire profile was measured within a clock accuracy of ± 0.01 s. In water, the glass-embedded NTC-Wien Bridge oscillator based T-sensors have response time of $\tau \approx 0.4$ s, a precision of < 0.5 mK and a noise level of < 0.1 mK (van Haren 2018). The time constant changes in air that has about 500 times smaller heat capacity than water. Environmental factors such as radiation effects may deteriorate the T-sensor signals. This is verified during a test experiment in Section 4.

As data transport is costly from remote deep-ocean areas, the T-sensors operate as stand-alone, running on a single Lithium AA-battery and storing data on a micro-SD-card. Lithium batteries have a flat response until a ‘sudden’ collapse upon draining, in contrast with exponentially decreasing power level in alkaline batteries of which the remaining power can always be monitored. Due to an error in bookkeeping of the sensor-use, the unknown remaining power in the sensors was considerably less than

expected. Already after two weeks sensors stopped and at the end of the 3 months of operation only 25% of the sensors worked. Here we consider only data from the first two weeks of operation, when at least 90% of sensors were operational. Missing data from non-operational sensors, and removed data from noisy sensors and sensors with calibration problems, are linearly interpolated between data from neighbouring sensors.

c. Post processing T-sensor data

Post-processing of the T-sensor data also involves correction for the non-randomly varying bias, which may be different for every sensor. For NTCs, this bias is basically due to their electronics drift. It is unknown what precisely causes the drift, even though it is often reported in temperature metrology. In the ocean, such a drift is noticed when measurements are made in waters with temperature variations in the mK-range showing horizontal bars in a time-depth image. Typical drifts are 1 mK/week initially and 1 mK/mo after aging of the NTCs.

The correction for drift can best be made when many sensors are mounted on a cable, in an environment that eventually is inherently stably stratified. Thus, we use an intrinsic property of natural water bodies that are heated from above. In such an environment, vertical T-profiles averaged over at least the buoyancy period should be stably stratified and, when averaged over all internal wave scales including the inertial period, should be smooth as well (van Haren and Gostiaux 2012). Any deviations from a smooth stably stratified mean profile are attributable to artificial drift, which is corrected for by subtracting a constant value per sensor. In practice, the averaging period varies, between the inertial period and several days, depending on the natural variation of stratification locally.

As we shall note below, this (drift) correction is difficult for measurements in air that are possibly affected by radiation effects. Even after correcting over periods as short as the buoyancy period during nocturnal observations, apparent drift or measurement bias remained, which was impossible to remove sensibly using the above method. Applying a correction using an averaging period shorter than buoyancy period would also remove genuine turbulent overturns and is thus not appropriate. This hampers quantification of turbulence values and the computation of vertical wavenumbers from T-sensors in air. It is noted that some qualitative turbulence results may still be inferred from spectral frequency analysis which is hardly affected by the bias.

For the present atmospheric experiment, raw T-data are transferred to potential temperature θ data to compensate for the dry adiabatic lapse rate $\Gamma_d = -dT/dz = g/c_p = 0.0098^\circ\text{C m}^{-1}$. We will mainly focus on periods when the relative humidity $<99\%$ so that the air is not saturated with moist. In this way, (dry air) potential temperature is a good tracer for density variations. Henceforth, we use the general wording of ‘temperature’ where we mean ‘potential temperature’. For practical convenience we will use the unit $^\circ\text{C}$ rather than K.

4. Test experiment

Prior to the mounting of the 197-m long cable we performed a test experiment in the Cabauw mast. The purpose of this test was to verify the possibility of measuring air temperature fluctuations with NIOZ T-sensors, to establish their response time in air, and to characterize radiation influences on the measured temperatures. Between 18 April and 5 July 2017, two T-sensors were mounted close to the sonic anemometer/thermometer at the tip of the southeast boom at 60 m (Fig. 2). The T-

sensors where mounted with their sensors oriented downward to decrease the influence of direct radiation as much as possible. As the T-sensors are taped to the cable we applied one sensor with black rubber near the sensor-head and the other with yellow tape to study possible changes in the radiation effects on the temperature measurements.

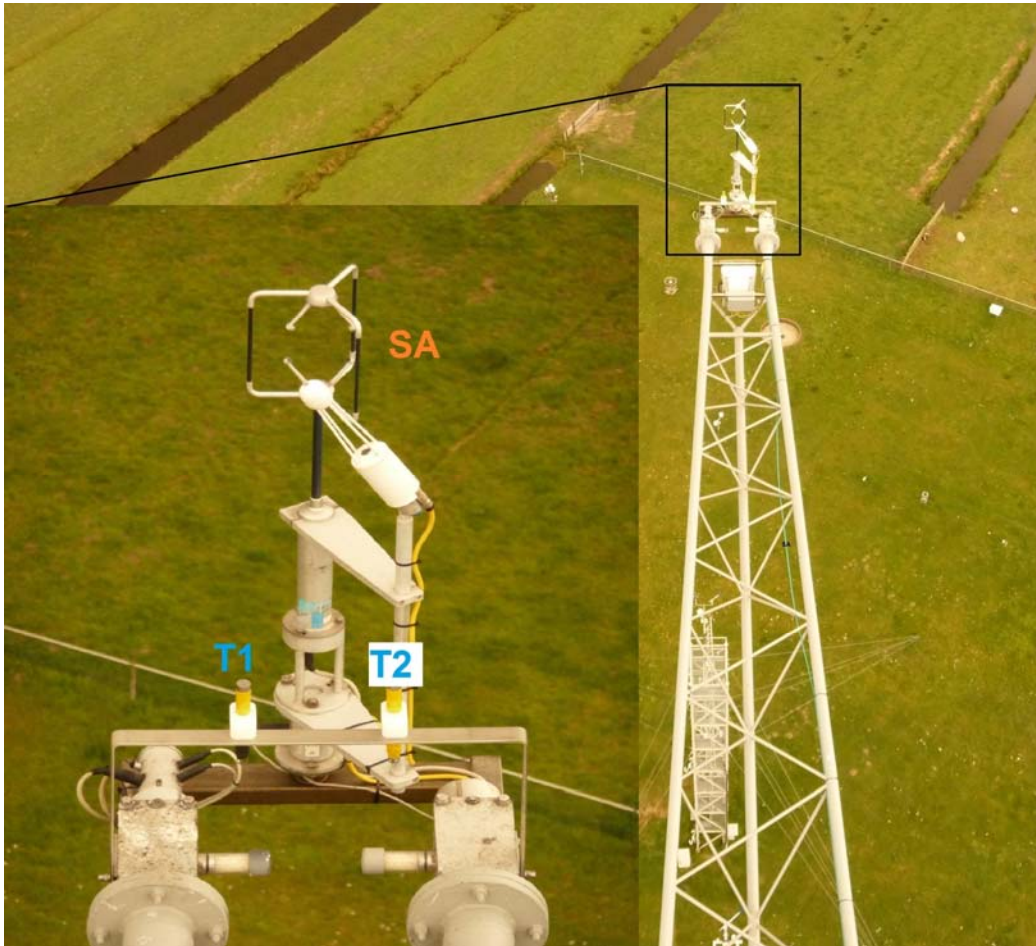


Fig. 2. Photos of the two downward pointing NIOZ4 T-sensors T_1 and T_2 mounted close to the sonic anemometer/thermometer SA at 60 m above ground on the tip of the SE-boom, during the test-experiment between 18 April and 5 July 2017.

During nocturnal periods, no bias was found between any of the three temperature records, and a very low noise level was observed between the two NIOZ T-sensors. During daytime, however, solar irradiation caused significant over-estimation of temperature. The T-sensor temperatures showed a fair amount of scatter in comparison with the standard reference temperature sensors of the mast at 40 and 80 m. This scatter was presumably due to varying irradiation due to clouds, and to varying shielding against solar radiation due to the specific configuration of the T-sensors and solar position. The different coatings of yellow tape and black rubber did not have any noticeable effect, as the two sensors did not show bias between them. Overall, the fast response sonic showed a smaller standard deviation of temperature fluctuations compared with the T-sensors during daytime periods, and a larger standard deviation during nocturnal periods. The former suggests a biased measurement of T-sensors during daytime referred to above. The latter points at a slower response time in the T-sensors. Henceforth we will mainly focus on nocturnal periods when the T-sensor performance was best and the standard deviation spread of noise error was about 0.015°C (Appendix).

Response times are verified using a two-day portion of the data, when skies were clear and wind direction was such that no interference with the tower was to be expected. The first day had low wind speeds $<4\text{ m s}^{-1}$, the second day moderate wind speeds $\sim 6\text{ m s}^{-1}$. Spectra were computed from the original 10-Hz-sampled sonic and the 1-Hz-sampled T-sensor data. Only the high-frequency two to three orders of magnitude are considered to establish the inertial subrange of turbulence with the well-known $-5/3$ power law (Tennekes and Lumley 1972). When plotted in a log-log fashion this provides a $-5/3$ slope, that is a $-2/3$ slope in an area preserving spectrum (Fig. 3a), which indeed fits the sonic data very well down to about 0.03 Hz (Fig. 3a).

The fit extends to the Nyquist frequency of the spectrum (5 Hz), which implies that the sonic response time is faster than 0.1 s, after accounting for aliasing.

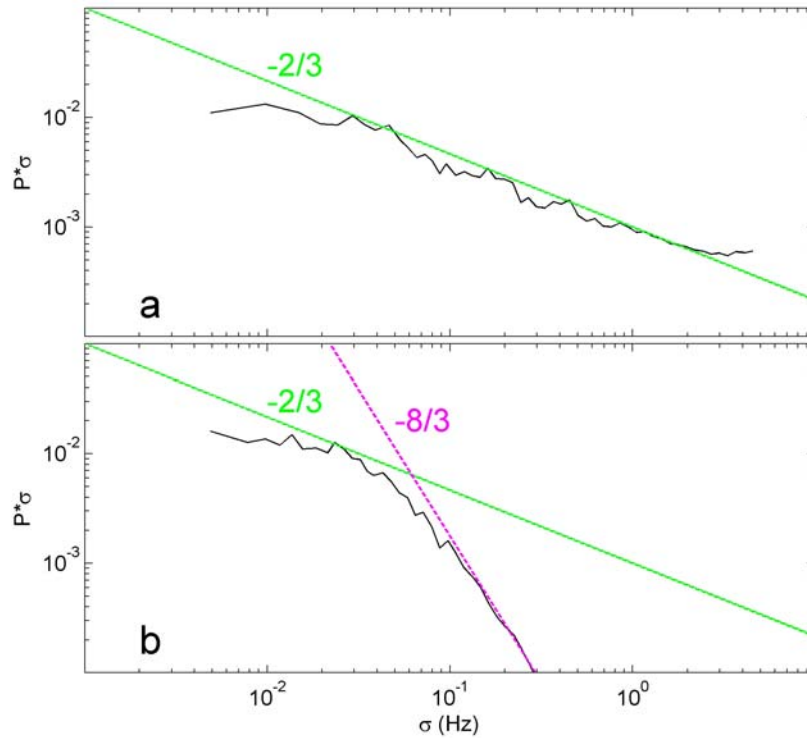


Fig. 3. 204 s mean nocturnal spectra to verify the inertial subrange ($\sigma^{-5/3}$ slope; represented by the straight solid line indicating the $-2/3$ power-law in log-log fashion of surface area preserving spectral form) and the time constant during the T-sensor test-experiment. (a) 10 Hz sonic data. (b) 1 Hz T-sensor data. The additional straight line indicates the $-8/3$ power-law that represents the $\sigma^{-11/3}$ slope of limited sensor response time.

The T-sensor data also demonstrate the inertial subrange, but over half to one order of magnitude only, down to about 0.01 Hz (Fig. 3b). At their high-frequency side they more rapidly, before 1 Hz, roll off fitting to about $-11/3$ slope, that is $-8/3$ in an area preserving spectrum due to incomplete sampling, in comparison with the

sonic spectrum. The two slopes (of $-2/3$ and $-8/3$) cross at about 0.06 Hz, which corresponds with a response time of $\tau \approx 3$ s for the T-sensors. No significant difference in τ - and inertial subrange determination was found between the two T-sensors, between daytime and nocturnal periods and between weak and moderate wind conditions.

The relatively slow response time of the NIOZ4 T-sensors in air implies that for typical wind speeds of 5 m s^{-1} scales of 15 m are resolved. This is quite different in water, where for typical 0.2 m s^{-1} current speeds length-scales of <0.1 m are resolved: Much less than the typical separation distance between the T-sensors on a string.

5. Results

a. Conditions overview

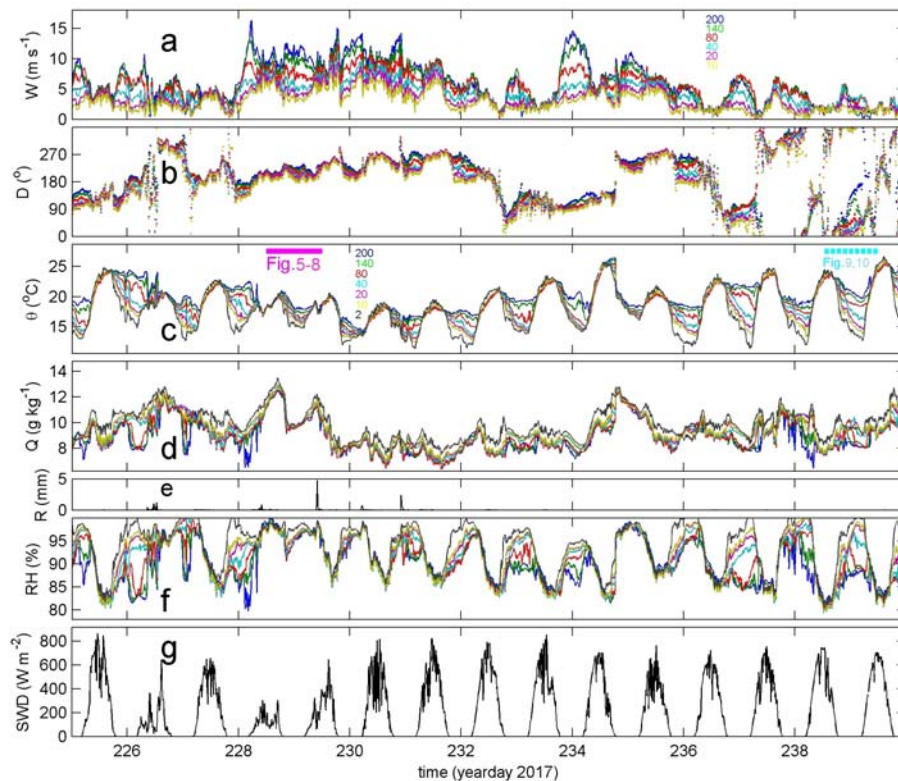


Fig. 4. 10-Minute sampled meteorological data overview of the first 15 days of T-string measurements. Indicated with different colours are measurements from

different heights level (in m, see legends in a. and c.). (a) Wind speed. (b) Wind direction, following the meteorological convention that 180° indicates wind coming from the South, ‘southerly wind’. (c) Potential temperature (for dry air), with horizontal bars indicating one day periods and detail-figure numbers. (d) Specific humidity (aka moisture content). (e) Rain fall observed at $z = 1$ m above ground. (f) Relative humidity. (g) Downward short-wave radiation observed at $z = 1$ m above ground.

An overview of the meteorological conditions during the first two weeks when the T-sensors were suspended in the mast is given in (Fig. 4). Wind speeds were $<15 \text{ m s}^{-1}$ (Fig. 4a). For investigation of a detailed magnification we selected periods when the wind direction was from the sector SE to SW (Fig. 4b), as during the first half of Fig. 4, so that the T-string was not in the wake of the tower. During nocturnal periods, surface cooling yielded a stable potential temperature stratification of typically $\Delta\theta = 4\text{-}8^\circ\text{C}$ over the $\Delta z = 197 \text{ m}$ range (Fig. 4c). During daytime, near-homogeneous temperatures were measured, although not permanently. During the week with (south-)westerly winds from sea, a few days of relatively large specific humidity (Fig. 4d) and light rain (Fig. 4e) were registered. Otherwise, days were without precipitation. Periods with $<100\%$ of relative humidity, of non-saturated air to avoid instrumental problems, occurred even for nocturnal periods (Fig. 4f). One of such nights with increased shear compared to daytime is selected for detailed investigation of T-sensor internal wave observations in Figs 5-8. A contrasting period with weaker easterly winds, less shear, stronger stratification but also $<100\%$ relative humidity will be presented in Figs 9-10.

b. Detailed observations: Moderate winds, strong shear

For detailed investigation of T-string data, we selected one day that is characterized by moderate southerly winds with relatively strong wind shear with speeds increasing after sunset at high levels and decreasing at low levels (Fig. 4a), with fairly high humidity including light rain in the beginning until day 228.55 and a small shower near the end at day 229.42 and overall relatively low downward short-wave radiation (Figs 4, 5). Across the 200 m vertical range of the mast, the one-day period is further characterized during the nocturnal period by: Relatively large wind speed variation ‘sheared wind’ from 3 m s^{-1} (at $z = 10 \text{ m}$) to 10 m s^{-1} (at $z = 200 \text{ m}$), moderate temperature variation ‘stratification’, no rain and small humidity change with height.

In the high-resolution T-string data, neutral to convective conditions occur as $\Delta\theta < 0.5^\circ\text{C}$ near-homogeneous temperature over the entire 197 m range (Fig. 5a, b). During daytime, besides convection, episodic weak stratification occurs of up to $N = 0.01 \text{ s}^{-1} \approx 140 \text{ cpd}$ (short for cycles per day) (Fig. 5c), under the notion that daytime T-sensor response may be biased.

About one-and-a-half hours before sunset, cooling from the ground, induced by negative net-radiation, starts a stable stratification rising upwards. This stratification increases in strength over time. About three hours before sunrise, temperature increases slightly at $z > 100 \text{ m}$ above ground, so that stratification increases as $z < 100 \text{ m}$ temperatures continue to decrease. About an hour before sunrise, minimum temperatures are reached at the lowest observational level. This more or less coincides with maximum stratification computed over the 197 m range. Subsequently, the stratification decreases due to the heating from below and, also, from above, but it is not reaching the low ‘daytime levels’ until 3 h after sunrise at day 229.35.

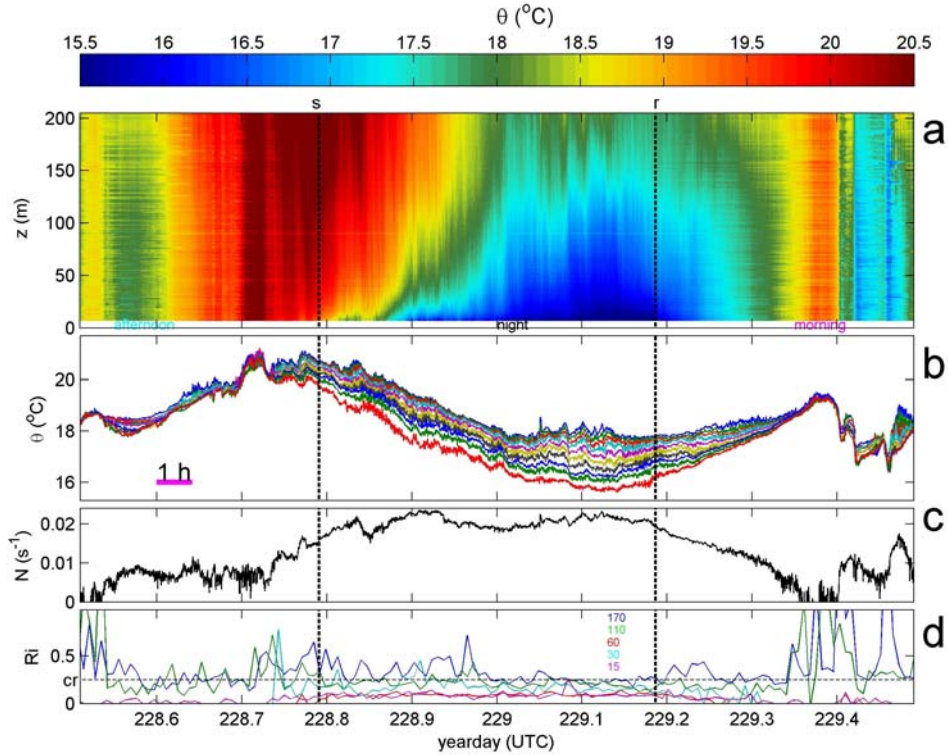


Fig. 5. One day example of T-string data during moderate southerly winds and little variation from 90 to 95% in relative humidity between daytime and nocturnal periods. Local times of sunrise ‘r’ and sunset ‘s’ are indicated by vertical black dashed lines. Time is in yeardays UTC, which is about 40 min behind local solar time LT. 23 T-sensors showed battery, noise or calibration problems. Their data are linearly interpolated from data of neighbouring sensors. (a) Time-depth series of potential temperature. The ground is at the horizontal axis. (b) Time series of potential temperature from height-levels every 20 m. (c) Time series of 197-m vertically averaged buoyancy frequency computed from upper and lower data in a., b. (d) Time series of gradient Richardson number Ri using (2) with atmospheric instrumentation data in Fig. 4, for five levels above ground as indicated in m. The horizontal dashed line indicates the critical level of 0.25, for one-dimensional shear flow.

During the night, the overall stratification rate yields a maximum 197-m averaged large-scale buoyancy frequency of $N \approx 0.022 \text{ s}^{-1} \approx 300 \text{ cpd}$, so that the shortest freely propagating internal waves have periods of about $T_N \approx 280 \text{ s}$. Despite this apparent stability, the destabilizing increased wind shear causes $Ri < 0.25$ over most of the vertical during most of the night, except for the upper 50 m up to day 229.0 (Fig. 5d).

1) FURTHER MAGNIFICATION AND VARYING STRATIFICATION

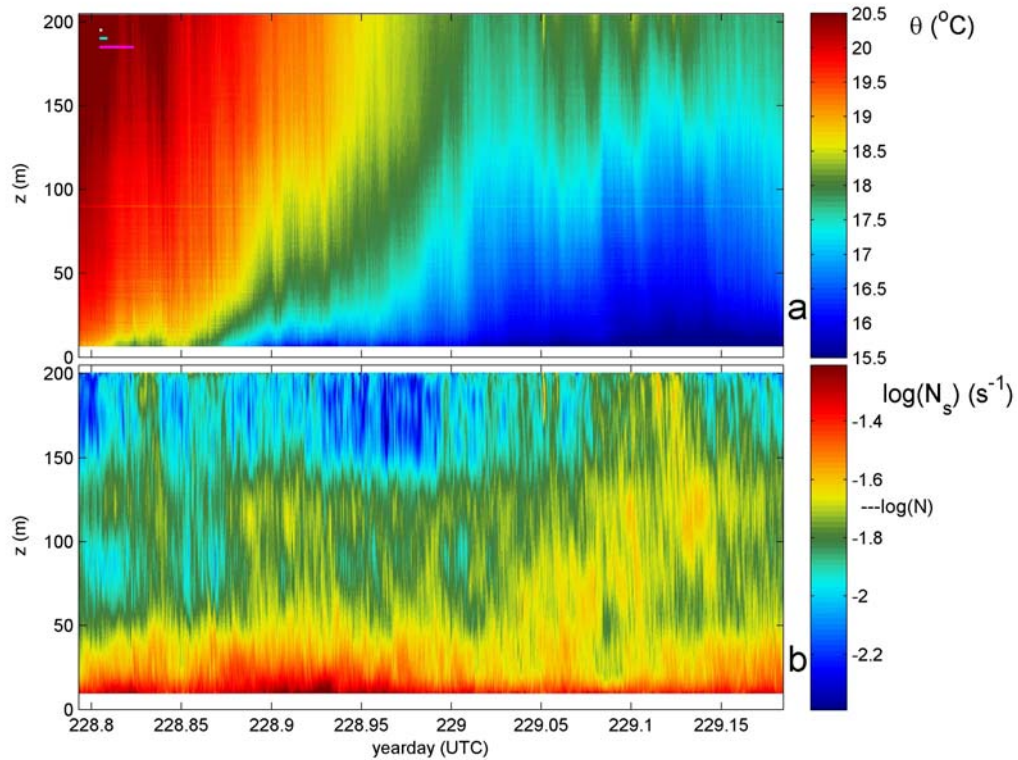


Fig. 6. (a) Nocturnal magnification of Fig. 5a. The white, blue and magenta bars in the upper-left corner reflect the duration of the shortest 1-m-scale, mean and overall minimum periods of freely propagating internal waves, respectively. (b) Logarithm of small-scale buoyancy frequency computed over 1 m intervals, averaged over 120 s, and smoothed over about 10 m using a 13th order polynomial. The value of the mean 197-m-large-scale buoyancy frequency is indicated by ‘-log(N)’.

When computed over shorter vertical scales of 1 m, local buoyancy frequency varies over one order of magnitude from about 0.06 to 0.006 s⁻¹ (800 to 80 cpd) between close to the ground and the highest mast levels (Fig. 6). We indicate the shortest buoyancy period in thin strongly stratified layers by the maximum 1-m small-scale buoyancy frequency $N_{s,max} \approx 800$ cpd and the longest buoyancy period in weakly stratified layers by $N_{min} \approx 80$ cpd. This allows small-scale 100 s internal waves to freely propagate in $z < 30$ m only, and which will be evanescent at higher levels.

In the magnification time-depth plot of temperature, shortest 1-m-small-scale, mean 197-m-large-scale and overall longest buoyancy periods are indicated by horizontal bars, for reference (Fig. 6a). The shortest buoyancy period indicates the smallest freely propagating internal wave period possible for the image plotted. It usually occurs nearest to the ground where local stratification is largest (Fig. 6b). Motions having ‘quasi-periods’ shorter than this shortest buoyancy period cannot, de facto, represent freely propagating internal waves, and likely represent a form of turbulent overturning. The longest buoyancy period reflects the highest frequency internal waves that certainly propagate freely supported by the minimum stratification in the domain plotted. Between the shortest and longest buoyancy periods, motions are expected to be a mix of freely propagating internal waves and episodic turbulent overturning.

2) SPECTRA

The atmospheric temperature variance spectra are not characterized by peaks, but by broadband signals that show various slopes with frequency (Fig. 7). In the spectrum of the particular night, the log-log-scale slope varies from approximately -2

at $\sigma < N_{\min}$, via $-7/5$ at $N_{\min} < \sigma < N$, (and possibly -1 at $N < \sigma < N_{s,\max}$), to $-5/3$ at $N_{s,\max} < \sigma < 3N_{s,\max} \approx$ roll-off due to limitations of the sensors' response time. It is noted that the strictly Eulerian fixed-in-space mast-observations do not Doppler shift frequencies of freely propagating internal waves, under the reasonable assumption that the wind-field does not transport the internal wave source (Gerkema et al., 2013). This will be demonstrated in the presentation of detailed observations during different wind conditions in Section 5c.

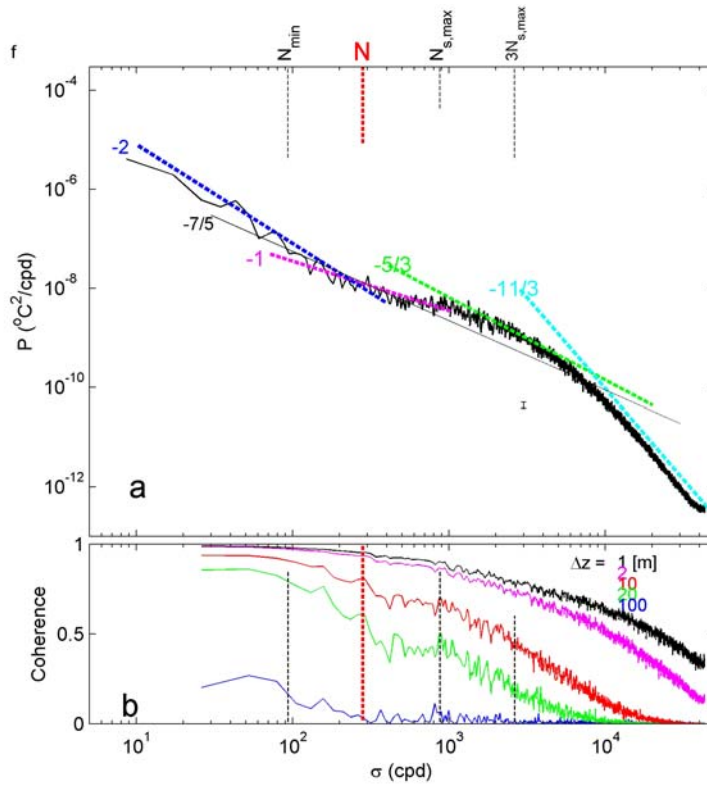


Fig. 7. Temperature spectra, averaged over all T-string sensors, for the nocturnal period of Fig. 5. (a) Power spectra of internal wave band and turbulence subranges. Different spectral slopes (for a log-log plot) are indicated, see text for explanation. (b) Corresponding coherence between all possible pairs of T-sensors at different mutual distances as indicated. The 95% significance level is approximately at coherence = 0.1.

In oceanography, a -2-slope reflects the canonical ocean-interior saturated internal wave slope for frequencies $f \ll \sigma \ll N$ (Garrett and Munk 1972). Recall that freely propagating internal waves are mostly expected in the frequency range $f \leq \sigma \leq N$ (f is to the outside left of Fig. 7a). The -7/5-slope, or the Bolgiano-Obukhov scaling, is known for an active scalar convective turbulence (e.g., Pawar and Arakiri 2016). Originally, this scaling was proposed for the buoyancy range of stratified turbulence, between the internal wave band and the inertial subrange (Bolgiano 1959). The -1-slope is equivalent to unsaturated, intermittent internal waves and has been observed close to N in the open-ocean (van Haren and Gostiaux 2009). The inertial subrange suggests a dominance of shear-induced turbulence for a passive scalar (Tennekes and Lumley 1972; Warhaft 2000). Shear production is thus expected at $\sigma < N_{s,max}$, either via internal wave shear including near-inertial wave shear, or via frictional boundary layer shear. The clearest change in spectral slope is seen at N , with a local hump around $N_{s,max}$.

For the nocturnal internal wave range at $\sigma < 80 \text{ cpd} \approx N_{min}$, coherence is found high with levels >0.8 between sensors at mutual distances of $\Delta z \leq 20 \text{ m}$ (Fig. 7b), while for $N \approx 300 < \sigma < 800 \text{ cpd} \approx N_{s,max}$ such high levels are only found for the shortest $\Delta z \leq 2 \text{ m}$. The former suggests little vertical phase differences, or local low-vertical-mode internal waves. The latter describes short-scale internal waves possibly supported by thin layer stratification. A small sub-peak is observed around $N_{s,max}$ for intermediate and larger scales, with further drop in coherence at higher frequencies. At $\sigma > 1000 \text{ cpd}$, the coherence levels roll off slowly, and they do not reach insignificance levels for the smallest vertical scales $\Delta z \leq 2 \text{ m}$ at the present Nyquist frequency. While this high-frequency end is far beyond the maximum freely

propagating internal wave frequency, and not well resolved by the slow T-sensors, its non-zero coherence does suggest that full 3D isotropic turbulence is not yet reached at frequencies of about 0.5 Hz, 4×10^4 cpd, during the nocturnal period.

3) FURTHER NOCTURNAL MAGNIFICATIONS

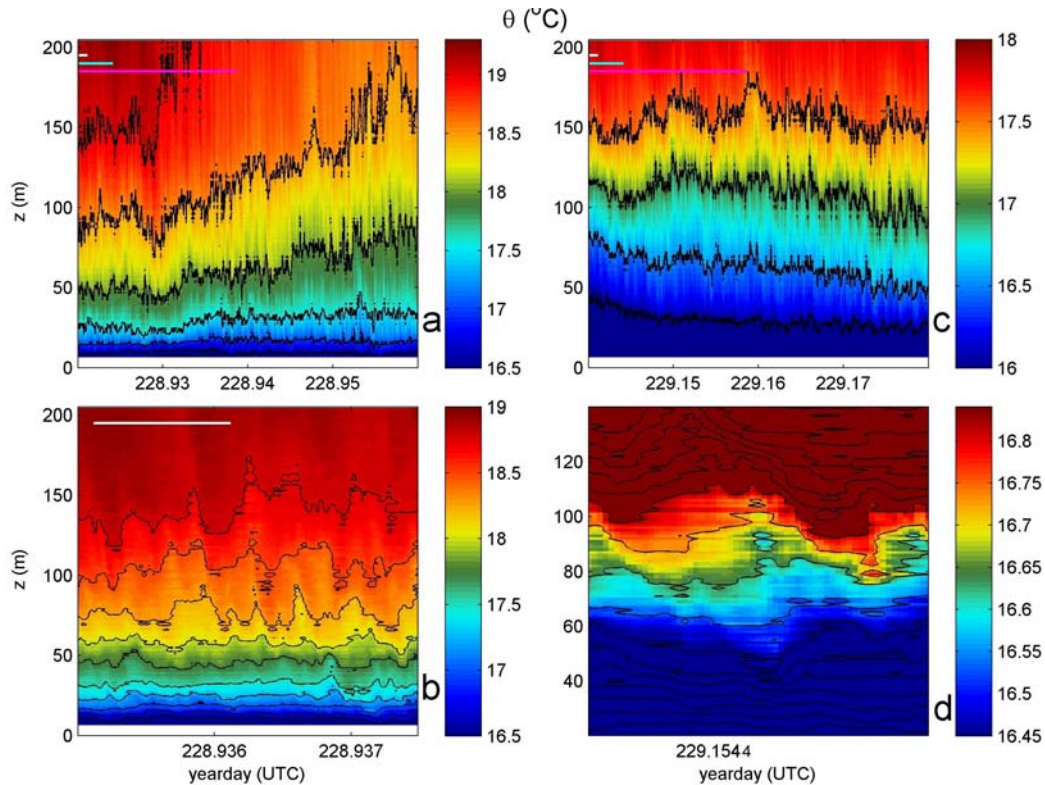


Fig. 8. Magnifications of nocturnal Fig. 6a with different colour ranges and black T-contours at different intervals. When the magnification window exceeds one or more buoyancy periods, the horizontal bars reflecting the periods are omitted. (a) One hour of data during 3 to 4 h after sunset. (b) A 220 s magnification of a. demonstrating apparent wave motions that have ‘periods’ smaller than the shortest small-scale buoyancy period (about 85 s; white bar) and a downward ‘phase’ propagation. (c) One hour of data during 1.5 to 0.5 h before sunrise with multiple high-frequency internal oscillations. (d) A 60 s magnification of c., indicating an apparent local vertical mode-2 internal oscillation with strong

suggestion of a Kelvin-Helmholtz billow due to shear instability of about 40 s duration and >20 m high.

The spectral observations are supported by further time-depth magnifications of the T-sensor data (Fig. 8). The nocturnal magnifications are dominated by apparent internal waves that are almost uniform over the 197-m vertical (Fig. 8a,c), having typically $O(10)$ m ‘amplitudes’ that vary throughout the domain and being largest for $z > 50$ m.

Further magnifications (Fig. 8b,d) demonstrate quasi-oscillatory motions that have periods shorter than the shortest buoyancy period (the white bar, which is longer than the 60 s of Fig. 8d). Such motions have a strongly nonlinear appearance, with an apparent downward ‘phase’ propagation. Although limited by the T-sensor resolution, regular small overturns (closed contours) are observed, and a likely suggestion for a KHi of shear-induced overturning in Fig. 8d. Quantification of the turbulent overturning is impossible, because of the T-sensors’ drift correction problems. The observed KHi does not form a roll-up billow, but merely a half-turn before collapsing. This is similar to ocean observations (van Haren and Gostiaux 2010).

c. Detailed observations on a day with weak wind and shear

The above one-day of late-summer observations was typical, but variations did occur between different days. Figs 9, 10, 11a show (details of) a day with strong short-wave radiation, with twice larger nocturnal stratification ($\sim N^2$) and weak north-easterly winds with little vertical shear.

Despite the different conditions, the observations in Fig. 9 show largely the same tendency as in Fig. 5. Exceptions are smaller high-frequency motions during

nocturnal stratification in the time series of Fig. 9b compared to Fig. 5b and larger Ri ($> Ri_{cr}$) for $z > 20$ m in Fig. 9d compared to Fig. 5d. During the nocturnal period, the T-spectrum of Fig. 10 is smoother than in Fig. 7. It has very similar -2 slope and variance content at $\sigma < N$, thus thereby extended over the range $[N_{min}, N]$ and demonstrating no effects of the different background advecting winds. A $-7/5$ slope of less variance is found at $N < \sigma < N_{s,max}$. The $-7/5$ slope is barely distinguishable from the $-5/3$ -slope with nearly one order of magnitude less variance for $\sigma > N_{s,max}$ than in Fig. 7. Less variance and no clear kink are also observed at $N_{s,max}$ in Fig. 10 compared with Fig. 7. Coherence is generally smaller in Fig. 10b than in Fig. 7b at all vertical intervals and frequencies, which suggests more relative dominance of higher-vertical-mode internal waves and smaller-scale vertical overturns.

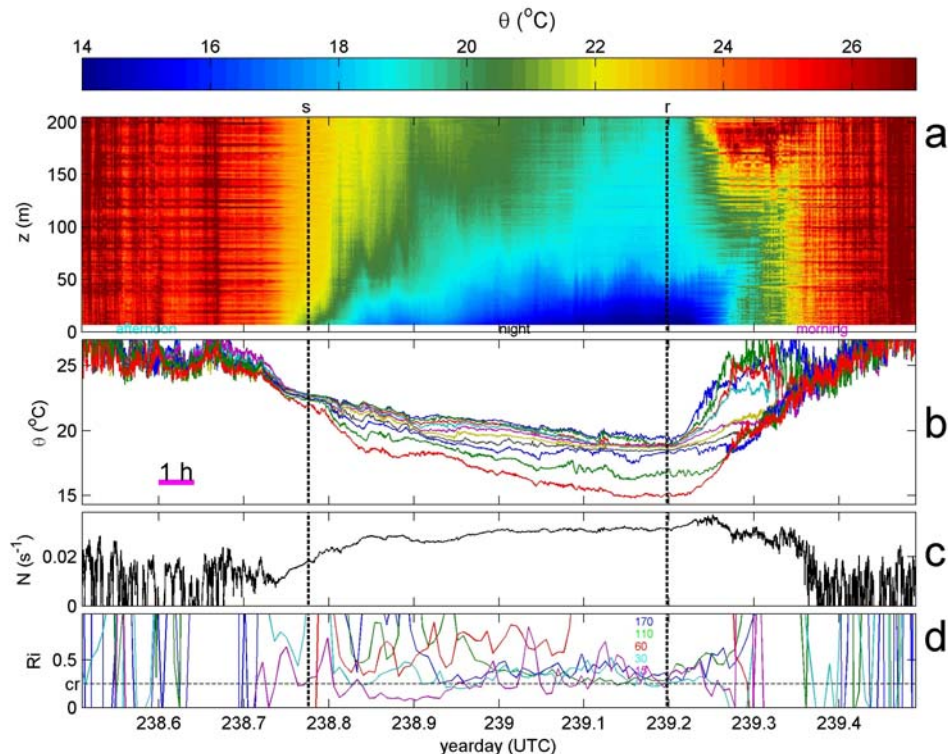


Fig. 9. As Fig. 5, but for a period 10 days later without rain, with strong daytime downward radiation, twice larger nocturnal stratification, weak north-easterly winds that are little sheared and less relative humidity except at ground level

where it reaches 100% during late night and visibility briefly is reduced to 500-1000 m. 38 T-sensors showed battery, noise or calibration problems. Their data are linearly interpolated from data of neighbouring sensors. Note the different scales in all panels compared with Fig. 5.

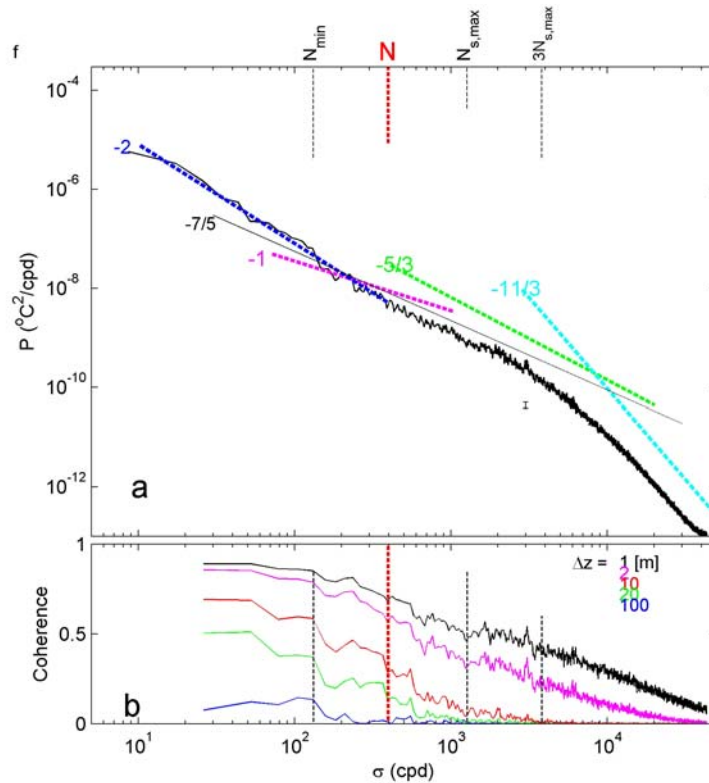


Fig. 10. As Fig. 7, but for nocturnal data in Fig. 9. The slopes are kept the same, for reference.

During the first 1.5 hours immediately after sunset, very high, super-buoyancy frequency quasi-turbulent motions are not observed in the depth-time domain of Fig. 11a, contrary to the period 10 days earlier (Fig. 11b). Stratification rises more quickly with time in Fig. 11a than in Fig. 11b and the internal waves have a linear appearance with variable periods $>T_N$ in Fig. 11a.

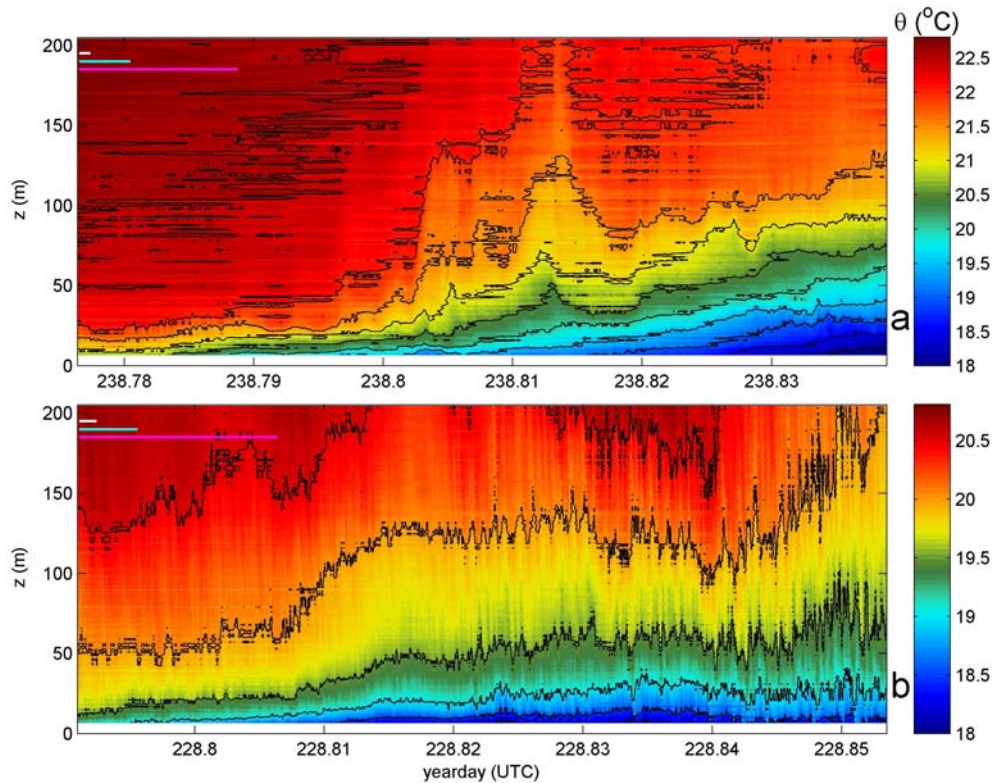


Fig. 11. Time-depth potential temperature details during 1.5 h immediately after sunset. In black, contours are given every 0.5°C . (a) From Fig. 9a when $Ri > 0.25$ for most of the vertical except for $z > 150$ m. (b) From Fig. 5a when $Ri < 0.25$ except for $z < 20$ m, with different colour scale.

6. Discussion and conclusions

Previous 10-min sampled meteorological observations have revealed the existence of internal waves in the stably stratified nocturnal atmospheric boundary layer (e.g., de Baas and Driedonks 1985). Such waves were considered to be generated for $Ri < 0.25$ in the lower levels above ground $z < 60$ m where the buoyancy period was smaller than 100 s (Duynderke 1991). It is surprising that observed much slower varying 40-min quasi-periodic motions could be trapped in this layer. Possibly, the near-ground shear essentially triggered unstable KHi that may have forced linear internal waves higher up in the troposphere, at frequencies well below N .

The present high-resolution observations demonstrate that quasi-periodic motions occur episodically throughout the nocturnal lower atmosphere. Such motions have periods that are shorter than the shortest possible buoyancy period and they have a strongly nonlinear appearance. They appear as spiky signals with vertical excursion $O(10\text{ m})$. Magnifications demonstrate they are either convective motions slanted to the vertical, or KHi demonstrating only half a turn before collapsing, which is similar to deep-ocean observations (van Haren and Gostiaux 2010).

The large-scale wind-shear, being enhanced at the beginning of the night, is found to drive Ri below the critical value of 0.25, a sufficient condition for linear instability. As a result, the apparently stably stratified nocturnal atmospheric boundary layer shows turbulent overturning during most of the summertime nights investigated. In contrast with the ocean, the large-scale wind/current-shear is the main driver of the instabilities in the stratified nocturnal atmospheric boundary layer.

During a, relatively rare, night on yearday 238/239 with low wind-shear, the above very high-frequency motions reflecting convection and/or KHi are few and linear internal waves dominate the observations. Also under these conditions however, $0.25 < Ri < 1$ suggests marginal stability, implying episodic vertical diapycnal mixing occurring, as found in the stratified North Sea (van Haren et al. 1999).

Unfortunately, the present high-resolution T-sensors demonstrate too large drift in air to be able to quantify the vertical turbulent exchange. However, the 1-Hz sampled 200 m vertical range does reveal abundant internal wave and stratified turbulence activity in the lower atmosphere, with large $>100\text{ m}$ vertical coherent scales for low internal wave frequencies $< 100\text{ cpd} \approx N_{\min}$, and small $<10\text{ m}$ scales for frequencies between $350\text{ cpd} \approx N$ and $1000\text{ cpd} \approx N_{s,\max}$. At higher frequencies, quasi-periodic motions appear as nonlinear waves, with turbulent overturning on the fringes that fill

the inertial subrange of shear-dominated turbulence. Even convection seems to occur in quasi-periodic episodes of 10-60 s also during nocturnal periods.

For future investigations it is suggested to find a means to improve the temperature observations. While the instrumental noise level of $<0.015^{\circ}\text{C}$ during nocturnal periods seems adequate, the T-sensors should be made more stable to avoid bias. Perhaps the sensor tip should be made smaller or of a different material, perhaps sampling the Wien bridge faster. Measurements would benefit from a faster response sensor with $\tau < 1$ s in air. If successful, it is expected that observations will also improve during the much stronger radiative daytime, possibly with the sensor in a small effective radiation shield.

Observational studies on the transition from large-scale shear flow, via (sheared) internal waves to instabilities leading to turbulence are still scarce, whether above a flat grassy field or in mountainous regions. Improved instrumentation will lead to more insight, qualitatively and quantitatively, that may also help to better parameterize large-scale atmospheric modelling. A distinction that may be made in such modelling is the variation in internal-wave-turbulence in the nocturnal boundary layer as a function of varying wind-shear. The present observations demonstrate the ubiquitous occurrence of internal waves of stable variance and spectral slope during nocturnal periods and their varying transition to turbulence in the lower atmosphere. The density-stratified nocturnal periods show episodic low stability via wind-shear that lead to convective overturning at relatively large vertical scales near the boundary. Marginal stability with little convection and smaller vertical scales near the boundary is found during nights when wind-shear is weak.

New observational techniques such as DTS are promising, although it is recommended for atmospheric boundary layer studies on internal waves and stratified

turbulence not to suspend the light-weight instrumentation from a balloon that moves too much under moderate wind speeds (Fritz 2019) but from a rigid mast. A short recent experiment (Peltola et al. 2021) from a 125 m mast above a forest showed DTS results with resolution, response time and noise levels very similar to the present observations. Longer duration experiments with such techniques may be well supplemented with higher resolution but shorter duration turbulence techniques such as sonic and profilers like TLS and Lidar (Frehlich et al. 2008).

Acknowledgements.

We thank A. Driever for the indispensable assistance in mounting and dismounting the T-sensor cable into the Cabauw-mast. The T-string was prepared with help from NIOZ-NMF. NIOZ temperature sensors have been financed in part by NWO, the Netherlands Organization for Scientific Research.

Data Availability Statement.

Requests for data can be directed to the corresponding author.

APPENDIX

Corrections, noise and genuine variability in T-profiles

During post-processing, the raw high resolution temperature data from Cabauw mast were transferred to physical units following a laboratory calibration in a custom-made bath that can hold up to 200 T-sensors. The calibration is performed in water, with the sensor tips in a titanium plate. The reference thermometer and the well-insulated bath ensure calibrations with a precision of about 0.0001°C (van Haren 2018). In air, the precision is much larger. However, the larger precision is not only due to electronic noise but also to poorly correctable drift, even for nocturnal profiles. As an example, the 2.4 h mean profile of uncorrected ‘raw’ temperature data demonstrates considerable ‘noise’ of small-scale temperature variations with a standard deviation spread of about 0.04°C (Fig. 12). This apparent noise is largely bias attributed to NTC-mismeasurement and a few large spikes. After drift-correction using a high-order polynomial fit and correcting for the dry adiabatic lapse rate, the ‘noise’ of small-scale temperature variations having a standard deviation spread of about 0.015°C in an individual potential temperature profile appears to be smaller than the spread of wiggles in the 2.4 h mean raw data profile. Despite this reduction in small-scale temperature variations, it remains unclear what part is due to measurement errors, and what part due to genuine atmospheric motions. Inspection of the 2.4 h mean and the individual potential temperature profiles demonstrates generally stably stratified profiles with warmer air above cooler air and a largest temperature gradient near the ground. Several tens of meters high wiggles in the individual potential temperature profile around the mean profile indicate internal wave oscillations. The question is whether the <10 m high unstable wiggles demonstrate genuine turbulent overturning.

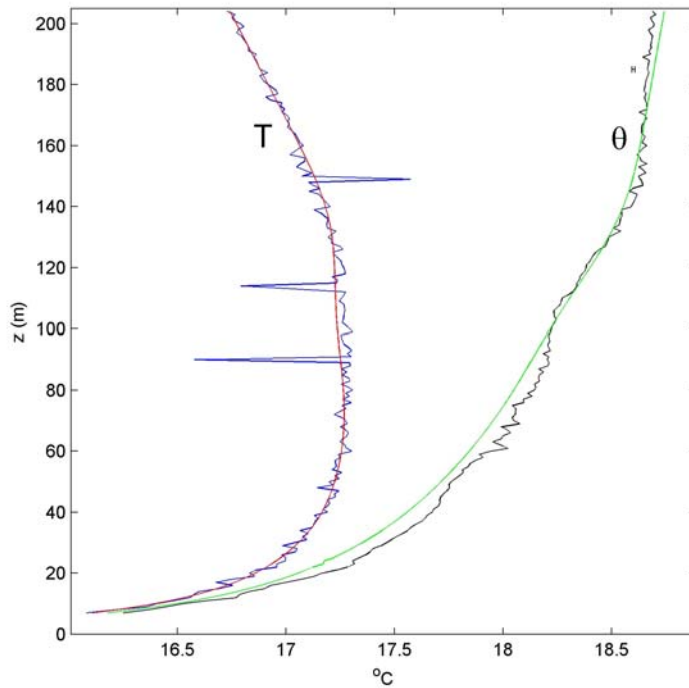


Fig. 12. Example of post-processing corrections for a vertical temperature profile. In blue, the measured temperature averaged over 2.4 h between nocturnal days 228.9 and 229.0. In red, its 13th order polynomial fit to correct all individual profiles for T-sensors drift. In black, a single individual profile of potential temperature at day 228.950 after drift- and dry adiabatic lapse rate corrections. The spread of small-scale temperature variations, ‘noise’ around the large-scale trend in the upper 30 m of the individual potential temperature is 0.015°C, as indicated by the small error-bar. In green, the 2.4 h average of potential temperature profiles.

REFERENCES

- Abarbanel, H. D. I., D.D. Holm, J. E. Marsden, and T. Ratiu, 1984: Richardson number criterion for the nonlinear stability of three-dimensional stratified flow. *Phys. Rev. Lett.*, **52**, 2352-2355.
- Akylas, T. R., 2010: *Gravity-wave dynamics in the atmosphere*. MIT-report, Cambridge, MA.
- Alexander, S. P., T. Tsuda, J. Furumoto, 2007: Effects of atmospheric stability on wave and energy propagation in the troposphere. *J. Atmos. Ocean. Technol.*, **24**, 602-615.
- Bolgiano, R., 1959): Turbulent spectra in a stably stratified atmosphere. *J. Geophys. Res.*, **64**, 2226-2229.
- Bosveld, F. C., and Coauthors, 2020 : Fifty years of atmospheric boundary-layer research at Cabauw serving weather, air quality and climate. *Bound.-Lay. Meteor.*, **177**, 583-612
- Burns, S. P., and J. Sun, 2000 : Thermocouple temperature measurements from the CASES-99 main tower. Preprints, 14th Symp. on Boundary Layer and Turbulence, Snowmass, CO, Amer. Meteor. Soc., 358-361.
- Carpenter, J. R., E. W. Tedford, E. Heifetz, G. A. Lawrence, 2011: Instability in stratified shear flow: Review of a physical interpretation based on interacting waves. *Appl. Mech. Rev.*, **64**, 060801.
- Conrck, R., C. F. Mass, and Q. Zhong, 2018: Simulated Kelvin-Helmholtz waves over terrain and their microphysical implications. *J. Atmos. Sci.*, **75**, 2787-2800.
- de Baas, A. F., and A. G. M. Driedonks, 1985: Internal gravity waves in a stably stratified boundary layer. *Bound.-Lay. Meteor.*, **31**, 303-323.

- Duynkerke, P. G., 1991: Observation of a quasi-periodic oscillation due to gravity waves in a shallow radiation fog. *Q. J. R. Meteor. Soc.*, **117**, 1207-1224.
- Eriksen, C. C., 1982: Observations of internal wave reflection off sloping bottoms. *J. Geophys. Res.*, **87**, 525-538.
- Finnigan, J. J., 1988: Kinetic energy transfer between internal gravity waves and turbulence. *J. Atmos. Sci.*, **45**, 525-505.
- Frehlich, R., Y. Meillier, and M. L. Jensen, 2008: Measurements of boundary layer profiles with in situ sensors and Doppler Lidar. *J. Atmos. Oceanic Technol.*, **25**, 1328-1340.
- Fritts, D. C., and M. J. Alexander, 2003: Gravity wave dynamics and effects in the middle atmosphere. *Rev. Geophys.*, **41**, 1003, doi:10.1029/2001RG000106.
- Fritz, A., 2019: Observation of the lower atmospheric boundary layer with fiber optic distributed sensing. BSc thesis, University Bayreuth, Germany, accessed 3 August 2021, http://www.bayceer.uni-bayreuth.de/meteo/de/top/diss/15/158822/BA_Antonia_Fritz.pdf.
- Garrett, C., and W. Munk, 1972: Space-time scales of internal waves. *Geophys. Fluid Dyn.*, **3**, 225-264.
- Gerkema, T., L. R. M. Maas, and H. van Haren, 2013: A note on the role of mean flows in Doppler shifted frequencies. *J. Phys. Oceanogr.*, **43**, 432-443.
- Gottelman, A., M. L. Salby, and F. Sassi, 2002: Distribution and influence of convection in the tropical tropopause region. *J. Geophys. Res.*, **107**, 4080, doi:10.1029/2001JD001048.
- Groen, P., 1948: Contribution to the theory of internal waves. *KNMI Med. Verh.*, **B11**, 1-23.

- Holtslag, A. A. M., and Coauthors, 2013: Stable atmospheric boundary layers and diurnal cycles: Challenges for weather and climate models. *Bull. Amer. Meteor. Soc.*, **November 2013**, 1691-1706
- Howard, L. N., 1961: Note on a paper of John W. Miles. *J. Fluid Mech.*, **10**, 509-512.
- Keller, C. A., and Coauthors, 2011: Fiber optic distributed temperature sensing for the determination of the nocturnal atmospheric boundary layer height. *Atmos. Meas. Tech.*, **4**, 143-149.
- La, I., and Coauthors, 2020: Influence of quasi-periodic oscillation of atmospheric variables on radiation fog over a mountainous region of Korea. *Atmosphere*, **11**, 230.
- LeBlond, P. H., and L. A. Mysak, 1978: *Waves in the Ocean*. Elsevier, 602 pp.
- Miles, J. W., 1961: On the stability of heterogeneous shear flows. *J. Fluid Mech.*, **10**, 496-508.
- Munk, W., and C. Wunsch, 1998: Abyssal recipes II: energetics of tidal and wind mixing. *Deep-Sea Res. I*, **45**, 1977-2010.
- Nappo, C. J., 2012: *An Introduction to Atmospheric Gravity Waves*. 2nd ed. Int. Geophys. Ser., 102, Academic Press, 400 pp.
- Nieuwstadt, F. T. M., 1984: The structure of the stable, nocturnal boundary layer. *J. Atmos. Sci.*, **41**, 2202-2216.
- Pawar, S. S., and J. H. Arakeri, 2016: Kinetic energy and scalar spectra in high Rayleigh number axially homogeneous buoyancy driven turbulence. *Phys. Fluids*, **28**, 065103.
- Peixoto, J. P., and A. H. Oort, 1992: *Physics of Climate*. AIP Press, 520 pp.

- Peltola, O., and Coauthors, 2021: Suitability of fiber-optic distributed temperature sensing to reveal mixing processes and higher-order moments at the forest-air interface. *Atmos. Meas. Tech.*, **14**, 2409-2427.
- Schenk, W. E., 1974: Cloud top height variability of strong convective cells. *J. Appl. Meteor.*, **13**, 917-922.
- Smyth, W. D., and J. N. Moum, 2012: Ocean mixing by Kelvin-Helmholtz instability. *Oceanography*, **25**, 140-149.
- Steenefeld, G.-J., C. J. Nappo, and A. A. M. Holtslag, 2009: Estimation of orographically induced wave drag in the stable boundary layer during the CASES-99 experimental campaign. *Acta Geophys.*, **57**, 857-881.
- Sun, J., and Coauthors, 2015: Review of wave-turbulence interactions in the stable atmospheric boundary layer. *Rev. Geophys.*, **53**, 956-993, doi:10.1002/2015RG000487.
- Sun, J., L. Mahrt, R. M. Banta, and Y. L. Pichugina, 2012: Turbulence regimes and turbulence intermittency in the stable boundary layer during CASES-99. *J. Atmos. Sci.*, **69**, 338-351.
- Tennekes, H., and J. L. Lumley, 1972: *A first course in turbulence*. MIT Press, 320 pp.
- Thorpe, S. A. 1987: Transitional phenomena and the development of turbulence in stratified fluids: a review. *J. Geophys. Res.*, **92**, 5231-5248.
- Tsuda, T., T. E. VanZandt, M. Mizumoto, S. Kato, and S. Fukao, 1991: Spectral analysis of temperature and Brunt-Väisälä frequency fluctuations observed by radiosondes. *J. Geophys. Res.*, **96**, 17,265-17,278.
- van Haren, H., 2018: Philosophy and application of high-resolution temperature sensors for stratified waters. *Sensors*, **18**, 3184, doi:10.3390/s18103184.

- van Haren, H., and L. Gostiaux, 2009: High-resolution open-ocean temperature spectra. *J. Geophys. Res.*, **114**, C05005, doi:10.1029/2008JC004967.
- van Haren, H., and L. Gostiaux, 2010: A deep-ocean Kelvin-Helmholtz billow train. *Geophys. Res. Lett.*, **37**, L03605, doi:10.1029/2009GL041890.
- van Haren H., and L. Gostiaux, 2012: Detailed internal wave mixing observed above a deep-ocean slope. *J. Mar. Res.*, **70**, 173-197.
- van Haren, H., L. Maas, J. T. F. Zimmerman, H. Ridderinkhof, and H. Malschaert, 1999: Strong inertial currents and marginal internal wave stability in the central North Sea. *Geophys. Res. Lett.*, **26**, 2993-2996.
- Xu, J., and Coauthors, 2007: Mesopause structure from thermosphere, ionosphere, mesosphere, energetics, and dynamics (TIMED)/sounding of the atmosphere using broadband emission radiometry (SABER) observations. *J. Geophys. Res.*, **112**, D09102, doi:10.1029/2006JD007711.
- Warhaft, Z. 2000: Passive scalars in turbulent flows. *Ann. Rev. Fluid Mech.*, **32**, 203-240.